Measurement of second order susceptibilities of GaN and AlGaN

N. A. Sanford[a)]
National Institute of Standards and Technology, Optoelectronics Division, MS 815, 325 Broadway, Boulder, Colorado 80305

A. V. Davydov
National Institute of Standards and Technology, Materials Science and Engineering Laboratory, 100 Bureau Drive, MS 8555 Gaithersburg, Maryland 20899

D. V. Tsvetkov and A. V. Dmitriev
TDI, Inc, Gaithersburg, Maryland 20904

S. Keller, U. K. Mishra, and S. P. DenBaars
Department of Electrical and Computer Engineering, University of California, Santa Barbara, Santa Barbara, California 93106

S. S. Park and J. Y. Han
Samsung Advanced Institute of Technology, P.O. Box 111, Suwon 440-600, Korea

R. J. Molnar
Lincoln Laboratory, Lexington, Massachusetts 02420

Rotational Maker fringes, scaled with respect to $\chi_{11}^{(2)}$ of crystalline quartz, were used to determine the second order susceptibilities $\chi_{31}^{(2)}$ and $\chi_{33}^{(2)}$ for samples of thin $Al_xGa_{1-x}N$ films, a thicker GaN film, and a free-standing GaN platelets. The pump wavelength was 1064 nm. The $Al_xGa_{1-x}N$ samples, ranging in thickness from roughly 0.5 to 4.4 μm, were grown by metalorganic chemical vapor deposition (MOCVD) and hydride vapor-phase epitaxy (HVPE) on (0001) sapphire substrates. The Al mole fractions x were 0, 0.419, 0.507, 0.618, 0.660, and 0.666, for the MOCVD-grown samples, and $x=0$, 0.279, 0.363, and 0.593 for the HVPE-grown samples. An additional HVPE-grown GaN sample ~ 70 μm thick was also examined. The free-standing bulk GaN platelets consisted of an HVPE grown film ~ 226 μm thick removed from its growth substrate, and a crystal ~ 160 μm thick grown by high-pressure techniques. For the $Al_xGa_{1-x}N$ samples, the magnitudes of $\chi_{31}^{(2)}$ and $\chi_{33}^{(2)}$ decrease roughly linearly with increasing x and extrapolate to ~ 0 for $x=1$. Furthermore, the constraint expected for a perfect wurtzite structure, namely $\chi_{33}^{(2)}=-2\chi_{31}^{(2)}$, was seldom observed, and the samples with $x=0.660$ and $x=0.666$ showed $\chi_{31}^{(2)}$ and $\chi_{33}^{(2)}$ having the same sign. These results are consistent with the theoretical studies of nonlinear susceptibilities for AlN and GaN performed by Chen *et al.* [Appl. Phys. Lett. **66**, 1129 (1995)]. The thicker bulk GaN samples displayed a complex superposition of high- and low-frequency Maker fringes due to the multiple-pass interference of the pump and second-harmonic generation beams, and the nonlinear coefficients were approximately consistent with those measured for the thin-film GaN sample. © *2005 American Institute of Physics*. [DOI: 10.1063/1.1852695]

I. INTRODUCTION

Methods of nonlinear optics (NLO) offer nondestructive means to probe and characterize bulk materials and thin films since the nonlinear optical interaction is necessarily dependent on structure, symmetry, and the presence of interfaces.[1] Applications of NLO techniques to the characterization of wide-band gap semiconductors include mapping SiC to reveal polytype formation, mapping of piezoelectric fields in III–nitrides, and the observation that rotational Maker fringes can reveal misoriented growth in nominally (0001) GaN films grown on sapphire substrates.[2–4] Furthermore, with their broad range of optical transparency and wurtzite structure, the wide-band gap III–nitrides may prove to be interesting materials with which to engineer nonlinear optical de-

vices based on guided-mode phase matching or quasiphase matching (QPM) techniques.[5,6] QPM is an elegant method of extending the phase-matching bandwidth of a nonlinear optical crystal by spatially modulating the magnitude or sign of the second-order susceptibility. This method has proven spectacularly successful in realizing efficient second harmonic generation (SHG) and optical parametric oscillation in such materials as $LiNbO_3$, $LiTaO_3$, and KTP.[6–8] Indeed, Miragliotta *et al.*[4] proposed a GaN-based QPM device based on an alternating stack of GaN and sapphire layers. More recently, growth of GaN on domain-engineered $LiNbO_3$ has permitted control of polarity in the GaN film.[9]

This emerging interest in GaN alloys as a material system in which to fabricate NLO devices also compels the study of the composition dependence of nonlinear optical coefficients discussed herein. In this article we describe the

a)Electronic mail: sanford@boulder.nist.gov

use of rotational Maker fringes to measure the nonlinear susceptibilities $\chi_{31}^{(2)}$ and $\chi_{33}^{(2)}$ of a series of $Al_xGa_{1-x}N$ samples grown by metalorganic chemical vapor deposition (MOCVD) and hydride vapor phase epitaxy (HVPE) on (0001) sapphire substrates. A free-standing bulk GaN platelet grown by high-pressure methods was also examined.

The $Al_xGa_{1-x}N$ thin films were typically 5 mm in cross section and ranged in thickness from roughly 0.5 to 4.4 μm. The values of the Al mole fraction x were 0.000, 0.419, 0.507, 0.618, 0.660, and 0.666, for the MOCVD-grown samples, and $x=0$, 0.279, 0.363, and 0.593 for an HVPE-grown samples. Details for these samples concerning crystal growth, calibration of the Al mole fraction x, and measurements of refractive index and birefringence are given elsewhere.[10] Least-squares methods were used to fit an analytical model describing rotational Maker fringes to experimental data collected from the samples. Our analysis includes both the full birefringence of the $Al_xGa_{1-x}N$ layer and growth substrate and the Fabry–Pérot resonances of the pump and second-harmonic fields. Scaling of the Maker fringe data with similar data collected from a crystalline quartz reference plate permitted calibration of $\chi_{31}^{(2)}$ and $\chi_{33}^{(2)}$ of the $Al_xGa_{1-x}N$ samples with respect to $\chi_{11}^{(2)}$ of the quartz reference plate. We observed a reduction in the magnitudes of $\chi_{31}^{(2)}$ and $\chi_{33}^{(2)}$ with increasing x. At $x=0$ $\chi_{31}^{(2)}$ =5.3 pm/V $\pm 8\%$ for the thin film MOCVD sample and $\chi_{31}^{(2)}=5.7$ pm/V $\pm 8\%$ for the thin HVPE sample. The magnitude of $\chi_{31}^{(2)}$ decreased in a roughly linear fashion to 1.6 pm/V for $x=0.666$. Over the same range of x the magnitude of $\chi_{33}^{(2)}$ also decreases. For example, at $x=0$ $\chi_{33}^{(2)}$ =−7.4 pm/V for the thin MOCVD grown sample and $\chi_{33}^{(2)}$ =−10.4 pm/V for the thin HVPE grown sample. At x =0.666 $\chi_{33}^{(2)}=3.9$ pm/V. In contrast with computations of $\chi_{31}^{(2)}$, the simulations reveal that the Maker fringes depend weakly on $\chi_{33}^{(2)}$ and the estimated uncertainty in $\chi_{33}^{(2)}$ is $\pm 40\%$ throughout. For a perfect wurtzite structure (class 6*mm*) one generally expects adherence to the constraint $\chi_{33}^{(2)}=-2\chi_{31}^{(2)}$.[4] However, we found that this relation was generally not obeyed for the set of samples examined. Additionally, for samples with $x \sim 0.6$, we found that $\chi_{31}^{(2)}$ and $\chi_{33}^{(2)}$ had the same sign, which is consistent with theoretical calculations of nonlinear susceptibilities in AlN films.[11] Thicker GaN samples were also examined. These consisted of an HVPE grown plate (roughly 230 μm thick) that was removed from its sapphire growth substrate, an HVPE grown film (roughly 70 μm thick) that remained on its growth substrate, and a bulk high-pressure grown platelet (roughly 160 μm thick). The HVPE grown samples were (0001) oriented and roughly 5 mm square. The bulk high-pressure grown GaN platelet was a (0001) oriented irregular hexagon measuring roughly 4 mm in cross section. Growth and preparation of these thicker GaN samples is discussed in Ref. 12. Compared to the thinner samples of $Al_xGa_{1-x}N$, these bulk samples displayed complex Maker fringe patterns of high-and low-frequency fringes because of the multiple Fabry–Pérot reflections of the pump and second harmonic generation (SHG) beams. The resolution of these high-frequency fringes is an indication of surface quality and uniformity of these thicker samples. The computed values for χ_{31} and χ_{33} were fairly consistent with those measured for the thin GaN film.

II. THEORY OF ROTATIONAL MAKER FRINGES IN GaN

A. Resonating pump fields in the GaN film

In order to properly treat the problem, the full Fabry–Pérot resonances of the pump and SHG must be considered. We first derive expressions for the forward- and backward-propagating pump fields in the GaN film and describe the conventions used in the treatment of wave propagation in anisotropic media. The experimental orientation of the GaN/sapphire sample, and the incident, reflected, forward, backward, and transmitted ordinary (*o*) and extraordinary (*e*) polarized pump fields are illustrated in Fig. 1(a). The incident and reflected pump fields at the air/GaN interface are represented by plane waves. The incident and reflected *o*-polarized pump fields are

$$\mathbf{E}_o^{pi} = \hat{y} E_y^{pi} \exp[i(\gamma_x x + \gamma_z z - \omega^p \tau)], \tag{1a}$$

$$\mathbf{E}_o^{pr} = \hat{y} E_y^{pr} \exp[i(\gamma_x x - \gamma_z z - \omega^p \tau)]. \tag{1b}$$

The incident and reflected *e*-polarized pump fields are

$$\mathbf{E}_e^{pi} = \{\hat{x} E_x^{pi} \exp[i(\gamma_x x + \gamma_z z)] + \hat{z} E_z^{pi} \exp[i(\gamma_x x + \gamma_z z)]\}$$
$$\times \exp(-i\omega^p \tau), \tag{2a}$$

$$\mathbf{E}_e^{pr} = \{\hat{x} E_x^{pi} \exp[i(\gamma_x x - \gamma_z z)] + \hat{z} E_z^{pi} \exp[i(\gamma_x x - \gamma_z z)]\}$$
$$\times \exp(-i\omega^p \tau), \tag{2b}$$

Throughout this article, boldface quantities represent vectors or tensors as the context indicates. Variables appearing in the preceding equations are identified as follows: τ is the time; ω^p and λ^p are, respectively, the angular frequency and vacuum wavelength of the pump field; $\gamma = 2\pi/\lambda^p$ is the magnitude of the wave vector for the pump field, with components $\gamma_x = \gamma \sin \theta_i$ and $\gamma_z = \gamma \cos \theta_i$. The *o*- or *e*-polarized pump fields in the GaN film and sapphire substrate are denoted by $\mathbf{E}_\beta^{p\alpha}$ and $\mathbf{H}_\beta^{p\alpha}$, where the superscript α may be assigned i, r, f^+, f^-, or t. Depending upon the context, the subscript β is assigned either o or e, indicating ordinary or extraordinary polarization. Here, the superscripts $f^\pm$ refer to propagation in the $\pm z$ direction in the GaN film. The superscript t refers to the propagation in the $+z$ direction through the sapphire substrate. The general dielectric tensor at wavelength λ^p referred to the principal axes of the $Al_xGa_{1-x}N$ or sapphire media is $\tilde{\boldsymbol{\varepsilon}}^{p\alpha} = \hat{x}\hat{x}(n_o^{p\alpha})^2 + \hat{y}\hat{y}(n_o^{p\alpha})^2 + \hat{z}\hat{z}(n_e^{p\alpha})^2$. Obviously, $n_o^{pf^+} = n_o^{pf^-} \equiv n_o^{pf}$, and $n_e^{pf^+} = n_e^{pf^-} \equiv n_e^{pf}$ in the $Al_xGa_{1-x}N$. Backward-propagating pump waves due to Fresnel reflection from the back of the sapphire substrate are ignored. Maxwell's equations for $\mathbf{E}_\beta^{p\alpha}$ and $\mathbf{H}_\beta^{p\alpha}$ are

$$\nabla \times \mathbf{E}_\beta^{p\alpha} = -\frac{\partial \mathbf{H}_\beta^{p\alpha}}{\partial \tau}, \tag{3a}$$

$$\nabla \times \mathbf{H}_\beta^{p\alpha} = \varepsilon_o \tilde{\boldsymbol{\varepsilon}}^{p\alpha} \cdot \frac{\partial \mathbf{E}_\beta^{p\alpha}}{\partial \tau}, \tag{3b}$$
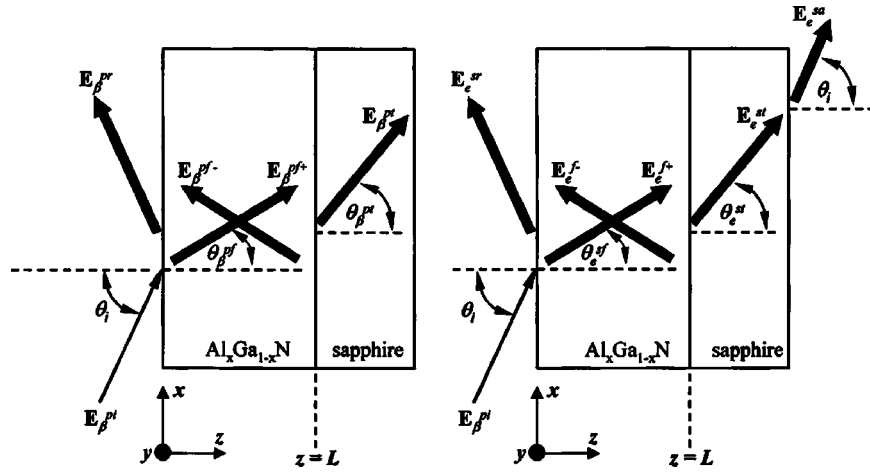
FIG. 1. (a) A schematic showing the incident pump field $\mathbf{E}_o^{\mathrm{pi}}$, the reflected pump field $\mathbf{E}_o^{\mathrm{pr}}$, the forward-propagating pump field in the $\mathrm{Al}_x\mathrm{Ga}_{1-x}\mathrm{N}$ film $\mathbf{E}_o^{\mathrm{pf}^+}$, the backward-propagating pump field in the film $\mathbf{E}_o^{\mathrm{pf}^-}$, and the pump field transmitted into the sapphire substrate $\mathbf{E}_o^{\mathrm{pt}}$. The subscript β is o for the o-e pumping configuration (pump polarization perpendicular to the incident plane) and e for the e-e pump configuration (pump polarization parallel to the incident plane). The heavy arrows indicate that the various pump fields result from resonant Fabry–Pérot buildup in the $\mathrm{Al}_x\mathrm{Ga}_{1-x}\mathrm{N}$ film. The pump angle of incidence θ_i is shown and the propagation angles $\theta_\beta^{\mathrm{pf}}$ and $\theta_\beta^{\mathrm{pt}}$ depend upon the pump orientation β. (b) Extraordinary-polarized SHG produced by either the o-e or e-e pumping configurations. The SHG field produced in reflection is $\mathbf{E}_e^{\mathrm{sr}}$, the forward- and backward-propagating SHG fields in the $\mathrm{Al}_x\mathrm{Ga}_{1-x}\mathrm{N}$ film are $\mathbf{E}_e^{f^+}$ and $\mathbf{E}_e^{f^-}$, respectively, the SHG field emerging into the sapphire substrate is $\mathbf{E}_e^{\mathrm{st}}$, and the SHG field exiting the substrate is $\mathbf{E}_e^{\mathrm{sa}}$. The propagation angles $\theta_\beta^{\mathrm{sf}}$ and $\theta_\beta^{\mathrm{st}}$ are also given and depend upon the pump orientation β. Heavy arrows indicate that the SHG fields results from Fabry–Pérot reflections of both the pump and SHG in the $\mathrm{Al}_x\mathrm{Ga}_{1-x}\mathrm{N}$ film. The $|\hat{c}|$ axes of the $\mathrm{Al}_x\mathrm{Ga}_{1-x}\mathrm{N}$ film and sapphire substrate are parallel to the $|\hat{z}|$ coordinate axis. The relative thickness of the $\mathrm{Al}_x\mathrm{Ga}_{1-x}\mathrm{N}$ film and sapphire substrate is not to scale in either (a) or (b).

$$\nabla \cdot (\varepsilon_o \widetilde{\boldsymbol{\varepsilon}}^{\mathrm{p}\alpha} \cdot \mathbf{E}_\beta^{\mathrm{p}\alpha}) = 0. \tag{3c}$$

These equations are used to derive wave equations that separately describe the o- or e-polarized pump fields in the birefringent media. In component form $E_y^{\mathrm{p}\alpha} = \hat{y} \cdot \mathbf{E}_o^{\mathrm{p}\alpha}$, $E_x^{\mathrm{p}\alpha} = \hat{x} \cdot \mathbf{E}_e^{\mathrm{p}\alpha}$, $E_z^{\mathrm{p}\alpha} = \hat{z} \cdot \mathbf{E}_e^{\mathrm{p}\alpha}$, and the wave equations become

$$\partial_{xx}^2 E_y^{\mathrm{p}\alpha} + \partial_{zz}^2 E_y^{\mathrm{p}\alpha} + (\gamma n_o^{\mathrm{p}\alpha})^2 = 0, \tag{4a}$$

$$(n_o^{\mathrm{p}\alpha})^2 \partial_{xx}^2 E_x^{\mathrm{p}\alpha} + (n_e^{\mathrm{p}\alpha})^2 \partial_{zz}^2 E_x^{\mathrm{p}\alpha} + (\gamma n_o^{\mathrm{p}\alpha} n_e^{\mathrm{p}\alpha})^2 = 0, \tag{4b}$$

$$(n_o^{\mathrm{p}\alpha})^2 \partial_{xx}^2 E_z^{\mathrm{p}\alpha} + (n_e^{\mathrm{p}\alpha})^2 \partial_{zz}^2 E_z^{\mathrm{p}\alpha} + (\gamma n_o^{\mathrm{p}\alpha} n_e^{\mathrm{p}\alpha})^2 = 0. \tag{4c}$$

The structure is uniaxial so the azimuthal orientation of the sample in Fig. 1 is immaterial, and the assignment of the crystal x and y axes, with the crystal y axis conforming to the laboratory y axis as shown in Figs. 1(a) and 1(b), is made purely for convenience.

The forward- and backward-propagating o-polarized pump fields in the GaN film are, respectively, $\mathbf{E}_o^{\mathrm{pf}^+}$ and $\mathbf{E}_o^{\mathrm{pf}^-}$. The forward-propagating pump field traversing the sapphire substrate is $\mathbf{E}_o^{\mathrm{pt}}$. These fields are represented by

$$\mathbf{E}_o^{\mathrm{pf}^+} = \hat{y} E_y^{\mathrm{pf}^+} \exp[i(\gamma_{xo}^f x + \gamma_{zo}^f z - \omega^p \tau)], \tag{5a}$$

$$\mathbf{E}_o^{\mathrm{pf}^-} = \hat{y} E_y^{\mathrm{pf}^-} \exp\{i[\gamma_{xo}^f x + \gamma_{zo}^f (L - z) - \omega^p \tau]\}, \tag{5b}$$

$$\mathbf{E}_o^{\mathrm{pt}} = \hat{y} E_y^{\mathrm{pt}} \exp\{i[\gamma_{xo}^f x + \gamma_{zo}^f (z - L) - \omega^p \tau]\}. \tag{5c}$$

The wave vector components for the o-polarized pump field are given by $\gamma_{xo}^f = n_o^{\mathrm{pf}} \gamma \sin \theta_o^{\mathrm{pf}}$, $\gamma_{zo}^f = n_o^{\mathrm{pf}} \gamma \cos \theta_o^{\mathrm{pf}}$, $\gamma_{xo}^f = n_o^{\mathrm{pt}} \gamma \sin \theta_o^{\mathrm{pt}}$, and $\gamma_{zo}^f = n_o^{\mathrm{pt}} \gamma \cos \theta_o^{\mathrm{pf}}$. The e-polarized pump fields in the GaN film and sapphire substrate are

$$\mathbf{E}_e^{\mathrm{pf}^+} = \{\hat{x} E_x^{\mathrm{pf}^+} \exp[i(\gamma_{xe}^f x + \gamma_{ze}^f z)] + \hat{z} E_z^{\mathrm{pf}^+} \exp[i(\gamma_{xe}^f x + \gamma_{ze}^f z)]\} \exp(-i\omega^p \tau), \tag{6a}$$

$$\mathbf{E}_e^{\mathrm{pf}^-} = [\hat{x} E_x^{\mathrm{pf}^-} \exp\{i[\gamma_{xe}^f x + \gamma_{ze}^f (L - z)]\} + \hat{z} E_z^{\mathrm{pf}^-} \exp\{i[\gamma_{xe}^f x + \gamma_{ze}^f (L - z)]\}] \exp(-i\omega^p \tau), \tag{6b}$$

$$\mathbf{E}_e^{\mathrm{pt}} = [\hat{x} E_x^{\mathrm{pt}} \exp\{i[\gamma_{xe}^f x + \gamma_{ze}^f (z - L)]\} + \hat{z} E_z^{\mathrm{pt}} \exp\{i[\gamma_{xe}^f x + \gamma_{ze}^f (z - L)]\}] \exp(-i\omega^p \tau). \tag{6c}$$

The wave vector components for the e-polarized pump fields appearing in Eqs. (6a)–(6c) are given by $\gamma_{xe}^f = n(\theta_e^{\mathrm{pf}}) \gamma \sin \theta_e^{\mathrm{pf}}$, $\gamma_{ze}^f = n(\theta_e^{\mathrm{pf}}) \gamma \cos \theta_e^{\mathrm{pf}}$, $\gamma_{xe}^f = n(\theta_e^{\mathrm{pt}}) \gamma \sin \theta_e^{\mathrm{pt}}$, and $\gamma_{ze}^f = n(\theta_e^{\mathrm{pt}}) \gamma \cos \theta_e^{\mathrm{pt}}$.

The factors

$$n(\theta_e^{\mathrm{pf}}) = n_e^{\mathrm{pf}} n_o^{\mathrm{pf}} \sqrt{1/[(n_e^{\mathrm{pf}} \cos \theta_e^{\mathrm{pf}})^2 + (n_o^{\mathrm{pf}} \sin \theta_e^{\mathrm{pf}})^2]}$$

and

$$n(\theta_e^{\mathrm{pt}}) = n_e^{\mathrm{pt}} n_o^{\mathrm{pt}} \sqrt{1/[(n_e^{\mathrm{pt}} \cos \theta_e^{\mathrm{pt}})^2 + (n_o^{\mathrm{pt}} \sin \theta_e^{\mathrm{pt}})^2]}$$

are, respectively, the extraordinary indices of refraction in the GaN layer and the sapphire substrate as functions of θ_e^{pf} and θ_e^{pt}. With the dependence of extraordinary index on pump angle of incidence so defined, one may readily verify that fields defined in Eqs. (5) and (6) satisfy Eqs. (4). Resonant buildup of the pump field in the sapphire substrate is neglected, and only the forward-propagating pump fields in the substrate $\mathbf{E}_o^{\mathrm{pt}}$ and $\mathbf{E}_e^{\mathrm{pt}}$ are retained. This is justified by considering that the sapphire substrates are typically ~0.4 mm thick, the $\mathrm{Al}_x\mathrm{Ga}_{1-x}\mathrm{N}$ films range in thickness from roughly 0.4 to 2.1 μm, and the diameter of the pump beam

incident upon a sample under test is approximately 70 μm. Considering these geometrical factors, pump resonance in the sapphire plate will occur only for θ_i within roughly $\pm 8°$ of normal incidence. As will be illustrated further on, within this narrow angular range the SHG intensity arising from the $Al_xGa_{1-x}N$ layer is typically negligible. However, given that the films are very thin compared to the pump-beam diameter, the pump resonance within the $Al_xGa_{1-x}N$ films should always be included in the analysis.

The continuity of the tangential components of the incident, resonating, and transmitted pump fields permits solution for the field amplitudes in terms of the incident amplitudes. Equation (3c) may be used to calculate the ratios of the x and z components of the e-polarized fields. The x- and y-polarized components of the magnetic field are calculated from Eq. (3a). With these in hand, one may then solve for the amplitudes of the forward and backward pump fields in the GaN film for both the o- and e-polarized pump cases. With $k_{zo}^{pf} = 2\gamma_{zo}^f$, the results for the o-polarized pump case are

$$E_y^{pf+} = \frac{T_o^i E_y^{pi}[1 + R_o^i R_o^t \exp(-ik_{zo}^{pf}L)]}{[1 + (R_o^i R_o^t)^2 + 2R_o^i R_o^t \cos(k_{zo}^{pf}L)]}, \tag{7a}$$

and

$$E_y^{pf-} = \frac{T_o^i R_o^t E_y^{pi}[1 + R_o^i R_o^t \exp(-ik_{zo}^{pf}L)]\exp(i\gamma_{zo}^f L)}{[1 + (R_o^i R_o^t)^2 + 2R_o^i R_o^t \cos(k_{zo}^{pf}L)]}, \tag{7b}$$

with

$$T_o^i = \frac{2\cos\theta_i}{n_o^{pf}\cos\theta_o^{pf} + \cos\theta_i}, \tag{8a}$$

$$R_o^i = \frac{n_o^{pf}\cos\theta_o^{pf} - \cos\theta_i}{n_o^{pf}\cos\theta_o^{pf} + \cos\theta_i}, \tag{8b}$$

$$R_o^t = \frac{n_o^{pt}\cos\theta_o^{pt} - n_o^{pf}\cos\theta_o^{pf}}{n_o^{pt}\cos\theta_o^{pt} + n_o^{pf}\cos\theta_o^{pf}}. \tag{8c}$$

Snell's laws for the o-polarized the pump are derived by considering continuity of the transverse phase at the boundaries $z=0$ and $z=L$ giving $\sin\theta_i = n_o^{pf}\sin\theta_o^{pf} = n_o^{pt}\sin\theta_o^{pt}$.

The x components of the forward- and backward-traveling e-polarized pump fields are

$$E_x^{pf+} = \frac{T_e^i E_x^{pi}[1 + R_e^i R_e^t \exp(-ik_{ze}^{pf}L)]}{[1 + (R_e^i R_e^t)^2 + 2R_e^i R_e^t \cos(k_{ze}^f L)]}, \tag{9a}$$

$$E_x^{pf-} = \frac{T_e^i R_e^t E_x^{pi}[1 + R_e^i R_e^t \exp(-ik_{ze}^{pf}L)]\exp(i\gamma_{ze}^f L)}{[1 + (R_e^i R_e^t)^2 + 2R_e^i R_e^t \cos(k_{ze}^{pf}L)]}, \tag{9b}$$

with $k_{ze}^{pf} = 2\gamma_{ze}^f$, and

$$T_e^i = \frac{2\cos\theta_e^{pf}}{\cos\theta_e^{pf} + n(\theta_e^{pf})\left[\left(\dfrac{n_o^{pf}}{n_e^{pf}}\sin\theta_e^{pf}\right)^2 + \cos^2\theta_e^{pf}\right]\cos\theta_i}, \tag{9c}$$

$$R_e^i = \frac{n(\theta_e^{pf})\left[\left(\dfrac{n_o^{pf}}{n_e^{pf}}\sin\theta_e^{pf}\right)^2 + \cos^2\theta_e^{pf}\right]\cos\theta_i - \cos\theta_e^{pf}}{n(\theta_e^{pf})\left[\left(\dfrac{n_o^{pf}}{n_e^{pf}}\sin\theta_e^{pf}\right)^2 + \cos^2\theta_e^{pf}\right]\cos\theta_i + \cos\theta_e^{pf}}, \tag{9d}$$

$$R_e^t = \frac{n(\theta_e^{pt})\left[\left(\dfrac{n_o^{pt}}{n_e^{pt}}\sin\theta_e^{pt}\right)^2 + \cos^2\theta_e^{pt}\right]\cos\theta_e^{pf} - n(\theta_e^{pf})\left[\left(\dfrac{n_o^{pf}}{n_e^{pf}}\sin\theta_e^{pf}\right)^2 + \cos^2\theta_e^{pf}\right]\cos\theta_e^{pt}}{n(\theta_e^{pf})\left[\left(\dfrac{n_o^{pf}}{n_e^{pf}}\sin\theta_e^{pf}\right)^2 + \cos^2\theta_e^{pf}\right]\cos\theta_o^{pt} + n(\theta_e^{pt})\left[\left(\dfrac{n_o^{pt}}{n_e^{pt}}\sin\theta_e^{pt}\right)^2 + \cos^2\theta_e^{pt}\right]\cos\theta_e^{pf}}. \tag{9e}$$

Snell's laws for the extraordinary pump case become $\sin\theta_i = n(\theta_e^{pf})\sin\theta_e^{pf} = n(\theta_e^{pt})\sin\theta_e^{pt}$.

B. Nonlinear wave equations

For hexagonal GaN (class $6mm$), we represent the second-order nonlinear susceptibility tensor $\chi_{ijk}^{(2)}$ in simplified matrix form by

$$\chi_{ij}^{(2)} = \begin{bmatrix} 0 & 0 & 0 & 0 & \chi_{15}^{(2)} & 0 \\ 0 & 0 & 0 & \chi_{24}^{(2)} & 0 & 0 \\ \chi_{31}^{(2)} & \chi_{32}^{(2)} & \chi_{33}^{(2)} & 0 & 0 & 0 \end{bmatrix}. \tag{10}$$

By symmetry considerations $\chi_{24}^{(2)} = \chi_{15}^{(2)}$ and $\chi_{31}^{(2)} = \chi_{32}^{(2)}$.[13,14] Additional simplification occurs with $\chi_{15}^{(2)} = \chi_{31}^{(2)}$, which may be derived by considering arguments based on the dispersion of the electronic contribution to the nonlinear susceptibility, or

by symmetry considerations.[15,16] Thus, we need consider only the two independent components $\chi_{31}^{(2)}$ and $\chi_{33}^{(2)}$. Furthermore, an additional constraint $\chi_{33}^{(2)} = -2\chi_{31}^{(2)}$ exists and is based on the premise that the optical nonlinearity in the hexagonal structure is due entirely to the contributions of tetrahedral units.[16] However, as discussed in Sec. III, this constraint was generally not experimentally verified. Note that we are representing the second-order susceptibility in SI units using the "$\chi_{ijk}^{(2)}$" convention rather than the "d_{ijk}" convention.[13,14] The dimensions of $\chi_{ijk}^{(2)}$ are pm/V and the numerical values of the coefficients between these conventions are related by $\chi_{ijk}^{(2)} = 2d_{ijk}$.

Returning to the sample orientation illustrated in Fig. 1, with the understanding that the coordinate axes in the AlGaN conform to the crystal axes, there are two cases of practical interest for the pump polarization that both produce

e-polarized SHG: (i) an *o*-polarized pump, resulting in a forward-propagating nonlinear source polarization $\mathbf{P}_{oe}^{f^+}$, the "*o-e*" case; and an *e*-polarized pump resulting in a forward-propagating nonlinear source polarization $\mathbf{P}_{ee}^{f^+}$; the "*e-e*" case. In simplified matrix form, these nonlinear source polarizations become

$$
\mathbf{P}_{oe}^{f^+} = \varepsilon_o
\begin{bmatrix}
0 & 0 & 0 & 0 & \chi_{31}^{(2)} & 0 \\
0 & 0 & 0 & \chi_{31}^{(2)} & 0 & 0 \\
\chi_{31}^{(2)} & \chi_{31}^{(2)} & \chi_{33}^{(2)} & 0 & 0 & 0
\end{bmatrix}
$$

$$
\times
\begin{bmatrix}
0 \\
(E_y^{pf^+})^2 \exp i(k_{xo}^{pf}x + k_{zo}^{pf}z) \\
0 \\
0 \\
0 \\
0
\end{bmatrix}
\times \exp(-i\omega\tau), \quad (11a)
$$

$$
\mathbf{P}_{ee}^{f^+} = \varepsilon_o
\begin{bmatrix}
0 & 0 & 0 & 0 & \chi_{31}^{(2)} & 0 \\
0 & 0 & 0 & \chi_{31}^{(2)} & 0 & 0 \\
\chi_{31}^{(2)} & \chi_{31}^{(2)} & \chi_{33}^{(2)} & 0 & 0 & 0
\end{bmatrix}
$$

$$
\times
\begin{bmatrix}
(E_x^{pf^+})^2 \exp i(k_{xe}^{pf}x + k_{ze}^{pf}z) \\
0 \\
(E_z^{pf^+})^2 \exp i(k_{xe}^{pf}x + k_{ze}^{pf}z) \\
0 \\
2E_z^{pf^+}E_x^{pf^+} \exp i(k_{xe}^{pf}x + k_{ze}^{pf}z) \\
0
\end{bmatrix}
\times \exp(-i\omega\tau),
$$

$$(11b)$$

where $\exp i(k_{x\beta}^{pf}x + k_{z\beta}^{pf}z - \omega\tau) = \exp 2i(\gamma_{x\beta}^f x + \gamma_{z\beta}^f z - \omega^p\tau)$. Thus, $\mathbf{P}_{oe}^{f^+}$ and $\mathbf{P}_{ee}^{f^+}$ will separately produce SHG polarized parallel to the laboratory *x* axes. Once again, our choice of the azimuthal orientation of the sample is not important. This may be verified by inspection of Eqs. (11a) and (11b), realizing that the *e* and *o* pump fields remain invariant under azimuthal rotation (e.g., rotation of the sample about an axis coincident with its surface normal). The symmetry of $\chi_{ijk}^{(2)}$ will always result in the same projections of the nonlinear source polarizations onto the *x* and *y* axes of the sample regardless of the azimuthal orientation of the sample with respect to the polarization axis of the pump. These assertions were verified experimentally by holding the sample at a fixed angle of incidence ($\theta_i \sim 40°$) and recording the SHG produced under *o-e* and *e-e* pumping conditions while the sample was rotated azimuthally about an axis parallel to the *c* axis. In all cases the azimuthal variation of the SHG was negligible. These observations further support the assumption that $\chi_{15}^{(2)} = \chi_{31}^{(2)}$.

The backward-propagating nonlinear source polarization $\mathbf{P}^{f^-}$ is similarly defined with the replacements of $f^+ \rightarrow f^-$ and $z \rightarrow (L-z)$ in Eqs. (11a) and (11b). All fields propagating

with vacuum wavelength λ and angular frequency ω are referred to as SHG fields. For the cases considered here, with the sample producing Maker fringes by rotation about the *y* axis, the SHG fields and the nonlinear source polarization are all *e* polarized while the pump fields are either *e* or *o* polarized (but not simultaneously *e* and *o* polarized). The forward-propagating SHG fields in the GaN film are denoted $\mathbf{E}_e^{f^+}$, $\mathbf{H}_e^{f^+}$, $\mathbf{P}_e^{f^+}$ and satisfy Maxwell's equations, where

$$
\nabla \times \mathbf{E}_e^{f^+} = -\mu_o \frac{\partial \mathbf{H}_e^{f^+}}{\partial\tau}, \quad (12a)
$$

$$
\nabla \times \mathbf{H}_e^{f^+} = \varepsilon_o \widetilde{\boldsymbol{\varepsilon}} \cdot \frac{\partial \mathbf{E}_e^{f^+}}{\partial\tau} + \frac{\partial \mathbf{P}_e^{f^+}}{\partial\tau}, \quad (12b)
$$

$$
\nabla \cdot (\varepsilon_o \widetilde{\boldsymbol{\varepsilon}}^{sf} \cdot \mathbf{E}_e^{f^+} + \mathbf{P}_e^{f^+}) = 0. \quad (12c)
$$

Analogous equations exist for the backward-propagating SHG fields. The respective ordinary and extraordinary indices of refraction at λ for the GaN film and the sapphire substrate are n_o^{sf}, n_e^{sf}, n_o^{st}, n_e^{st}. The dielectric tensors in these media are

$$
\widetilde{\boldsymbol{\varepsilon}}^{sf} = \hat{x}\hat{x}(n_o^{sf})^2 + \hat{y}\hat{y}(n_o^{sf})^2 + \hat{z}\hat{z}(n_e^{sf})^2,
$$

and

$$
\widetilde{\boldsymbol{\varepsilon}}^{st} = \hat{x}\hat{x}(n_o^{st})^2 + \hat{y}\hat{y}(n_o^{st})^2 + \hat{z}\hat{z}(n_e^{st})^2.
$$

C. *e*-polarized SHG arising from an *o*-polarized pump field

Manipulation of Eqs. (12a)–(12c) leads directly to a wave equation describing the SHG field $\mathbf{E}_e^{f^+}$ for the *o-e* case. The forward-propagating SHG field in the GaN film is $\mathbf{E}_e^{f^+}$, where $\mathbf{E}_e^{f^+} = \hat{x}E_x^{f^+} + \hat{z}E_z^{f^+}$ and the SHG field components $E_x^{f^+}$ and $E_z^{f^+}$ satisfy

$$
(n_o^{sf})^2 \partial_{xx}^2 E_x^{f^+} + (n_e^{sf})^2 \partial_{zz}^2 E_x^{f^+} + (kn_e^{sf}n_o^{sf})^2 E_x^{f^+}
$$
$$
= \tfrac{1}{2}\chi_{31}^{(2)} \sin(2\theta_o^{pf})(kn_o^{pf}E_y^{pf^+})^2 \exp i(k_{xo}^{pf}x + k_{zo}^{pf}z - \omega\tau), \quad (13a)
$$

$$
(n_o^{sf})^2 \partial_{xx}^2 E_z^{f^+} + (n_e^{sf})^2 \partial_{zz}^2 E_z^{f^+} + (kn_e^{sf}n_o^{sf})^2 E_z^{f^+}
$$
$$
= \chi_{31}^{(2)}[(n_o^{pf} \cos\theta_o^{pf})^2 - (n_o^{sf})^2](kE_y^{pf^+})^2
$$
$$
\times \exp i(k_{xo}^{pf}x + k_{zo}^{pf}z - \omega\tau). \quad (13b)
$$

Similarly, $\mathbf{E}_e^{f^-} = \hat{x}E_x^{f^-} + \hat{z}E_z^{f^-}$, where the SHG field components $E_x^{f^-}$ and $E_z^{f^-}$ satisfy

$$
(n_o^{sf})^2 \partial_{xx}^2 E_x^{f^-} + (n_e^{sf})^2 \partial_{zz}^2 E_x^{f^-} + (kn_e^{sf}n_o^{sf})^2 E_x^{f^-}
$$
$$
= -\tfrac{1}{2}\chi_{31}^{(2)} \sin(2\theta_o^{pf})(kn_o^{pf}E_y^{pf^-})^2
$$
$$
\times \exp i[k_{xo}^{pf}x + k_{zo}^{pf}(L-z) - \omega\tau], \quad (13c)
$$

$$
(n_o^{sf})^2 \partial_{xx}^2 E_z^{f^-} + (n_e^{sf})^2 \partial_{zz}^2 E_z^{f^-} + (kn_e^{sf}n_o^{sf})^2 E_z^{f^-}
$$
$$
= \chi_{31}^{(2)}[(n_o^{pf} \cos\theta_o^{pf})^2 - (n_o^{sf})^2](kE_y^{pf^-})^2
$$
$$
\times \exp i[k_{xo}^{pf}x + k_{zo}^{pf}(L-z) - \omega\tau]. \quad (13d)
$$

The general solutions to Eqs. (13a)–(13d) are

$$E_x^{f^+} = E_x^{f_o^+} \exp i(k_{xe}^{sf}x + k_{ze}^{sf}z - i\omega\tau)$$
$$+ A_x^+ \exp i(k_{xo}^{pf}x + k_{zo}^{pf}z - i\omega\tau), \tag{14a}$$

$$E_z^{f^+} = E_z^{f_o^+} \exp i(k_{xe}^{sf}x + k_{ze}^{sf}z - i\omega\tau)$$
$$+ A_z^+ \exp i(k_{xo}^{pf}x + k_{zo}^{pf}z - i\omega\tau), \tag{14b}$$

$$E_x^{f^-} = E_x^{f_o^-} \exp i[k_{xe}^{sf}x + k_{ze}^{sf}(L - z) - i\omega\tau]$$
$$+ A_x^- \exp i[k_{xo}^{pf}x + k_{zo}^{pf}(L - z) - i\omega\tau], \tag{14c}$$

$$E_z^{f^-} = E_z^{f_o^-} \exp i[k_{xe}^{sf}x + k_{ze}^{sf}(L - z) - i\omega\tau]$$
$$+ A_z^- \exp i[k_{xo}^{pf}x + k_{zo}^{pf}(L - z) - i\omega\tau], \tag{14d}$$

where $k_{xe}^{sf} = kn(\theta_e^{sf})\sin\theta_e^{sf}$, $k_{ze}^{sf} = kn(\theta_e^{sf})\cos\theta_e^{sf}$, and $n(\theta_e^{sf}) = n_e^{sf}n_o^{sf}\sqrt{1/[(n_e^{sf}\cos\theta_e^{sf})^2 + (n_o^{sf}\sin\theta_e^{sf})^2]}$. The coefficients A_x^+, A_z^+, A_x^-, A_z^- of the particular solutions are

$$A_x^+ = \frac{\chi_{31}^{(2)}(E_y^{pf^+})^2\sin 2\theta_o^{pf}}{2[(n_e^{sf}n_o^{sf}/n_o^{pf})^2 - (n_e^{sf}\cos\theta_o^{pf})^2 - (n_o^{sf}\sin\theta_o^{pf})^2]}, \tag{15a}$$

$$A_z^+ = \frac{\chi_{31}^{(2)}[(\cos\theta_o)^2 - (n_o^{sf}/n_o^{pf})^2](E_y^{pf^+})^2}{[(n_e^{sf}n_o^{sf}/n_o^{pf})^2 - (n_e^{sf}\cos\theta_o^{pf})^2 - (n_o^{sf}\sin\theta_o^{pf})^2]}, \tag{15b}$$

$$A_x^- = -A_x^+(R_o^t)^2, \tag{15c}$$

$$A_z^- = A_z^+(R_o^t)^2. \tag{15d}$$

The *e*-polarized SHG field generated in reflection from the air/GaN interface is $\mathbf{E}_e^{sr}$, and the *e*-polarized SHG field transmitted into the substrate is $\mathbf{E}_e^{st}$. These fields are given by

$$\mathbf{E}_e^{sr} = \{\hat{x}E_x^{sr}\exp[i(k_x x - k_z z)] + \hat{z}E_z^{sr}\exp[i(k_x x - k_z z)]\}$$
$$\times \exp(-i\omega\tau), \tag{16a}$$

$$\mathbf{E}_e^{st} = \{\hat{x}E_x^{st}\exp[i(k_{xe}^{st}x + k_{ze}^{st}z)] + \hat{z}E_z^{st}\exp[i(k_{xe}^{st}x + k_{ze}^{st}z)]\}$$
$$\times \exp(-i\omega\tau), \tag{16b}$$

where the wave vector components $k_{xe}^{st} = n(\theta_e^{st})k\sin\theta_e^{st}$, $k_{ze}^{st} = n(\theta_e^{st})k\cos\theta_e^{st}$, with $n(\theta_e^{st}) = n_e^{st}n_o^{st}/\sqrt{(n_e^{st}\cos\theta_e^{st})^2 + (n_o^{st}\sin\theta_e^{st})^2}$. The solution of the reflected, circulating, and transmitted SHG field amplitudes are found by application of the boundary conditions that require the continuity of the tangential components of the SHG fields at $z = 0, L$, where

$$\hat{x} \cdot \mathbf{E}_e^{sr}|_{z=0} = \hat{x} \cdot (\mathbf{E}_e^{f^+} + \mathbf{E}_e^{f^-})|_{z=0}, \tag{17a}$$

$$\hat{y} \cdot \nabla \times \mathbf{E}_e^{sr}|_{z=0} = \hat{y} \cdot \nabla \times (\mathbf{E}_e^{f^+} + \mathbf{E}_e^{f^-})|_{z=0}, \tag{17b}$$

$$\hat{x} \cdot \mathbf{E}_e^{st}|_{z=L} = \hat{x} \cdot (\mathbf{E}_e^{f^+} + \mathbf{E}_e^{f^-})|_{z=L}, \tag{17c}$$

$$\hat{y} \cdot \nabla \times \mathbf{E}_e^{st}|_{z=L} = \hat{y} \cdot \nabla \times (\mathbf{E}_e^{f^+} + \mathbf{E}_e^{f^-})|_{z=L}. \tag{17d}$$

In the solution of Eq. (17a)–(17d), we are concerned only with solving for the SHG field $\mathbf{E}_e^{st}$. Clearly, $E_z^{sa} = -E_x^{sa}\tan\theta_i$,

and the SHG field leaving the substrate for $z \geq L$ is $\mathbf{E}_e^{sa} = E_x^{sa}(\hat{x} - \hat{z}\tan\theta_i)\exp[i(k_x x + k_z(z - L) - \omega\tau)]$. The Fresnel transmission coefficient T_e^s links $\mathbf{E}_e^{st}$ and $\mathbf{E}_e^{sa}$ via $E_x^{sa} = T_e^s E_x^{st}$, where

$$T_e^s = \frac{2\left[\left(\dfrac{n_o^{st}\sin\theta_e^{st}}{n_e^{st}}\right)^2 + \cos^2\theta_e^{st}\right]n(\theta_e^{st})\cos\theta_i}{2\left[\left(\dfrac{n_o^{st}\sin\theta_e^{st}}{n_e^{st}}\right)^2 + \cos^2\theta_e^{st}\right]n(\theta_e^{st})\cos\theta_i + \cos\theta_e^{st}}. \tag{18}$$

The normalized *e*-polarized SHG power leaving the substrate for the *o*-*e* case is defined as $\mathbf{P}_{oe}^A = |\mathbf{E}_e^{sa}|^2$. An explicit form of $|\mathbf{E}_e^{sa}|^2$ is given in Appendix A.

D. *e*-polarized SHG arising from an *e*-polarized pump field

Following a procedure similar to that used in the last section, we may derive a set of wave equations that describe the generation of *e*-polarized SHG when only an *e*-polarized pump field is present. The forward-propagating SHG field is given by the solutions to the equations

$$(n_o^{sf})^2\partial_{xx}^2 E_x^{f^+} + (n_e^{sf})^2\partial_{zz}^2 E_x^{f^+} + (kn_e^{sf}n_o^{sf})^2 E_x^{f^+}$$
$$= (E_x^{pf^+})^2\chi_{31}^{(2)}k^2\Bigg\{[(n_e^{sf})^2 - (n(\theta_e^{sf})\sin\theta_e^{pf})^2]2\left(\frac{n_o^{pf}}{n_e^{pf}}\right)^2\tan\theta_e^{pf}$$
$$+ [n(\theta_e^{pf})]^2\left\{1 + \frac{\chi_{33}^{(2)}}{\chi_{31}^{(2)}}\left[\left(\frac{n_o^{pf}}{n_e^{pf}}\right)^2\tan\theta_e^{pf}\right]^2\right\}\cos\theta_e^{pf}\sin\theta_e^{pf}\Bigg\}$$
$$\times \exp i(k_{xe}^{pf}x + k_{ze}^{pf}z - \omega\tau), \tag{19a}$$

and

$$(n_o^{sf})^2\partial_{xx}^2 E_z^{f^+} + (n_e^{sf})^2\partial_{zz}^2 E_z^{f^+} + (kn_e^{sf}n_o^{sf})^2 E_z^{f^+}$$
$$= (E_x^{pf^+})^2\chi_{31}^{(2)}k^2\Bigg\{\left\{1 + \frac{\chi_{33}^{(2)}}{\chi_{31}^{(2)}}\left[\left(\frac{n_o^{pf}}{n_e^{pf}}\right)^2\tan\theta_e^{pf}\right]^2\right\}$$
$$\times [(n(\theta_e^{pf})\cos\theta_e^{pf})^2 - (n_o^{sf})^2]$$
$$- 2\left[\frac{n(\theta_e^{pf})n_o^{pf}\sin\theta_e^{pf}}{n_e^{pf}}\right]^2\Bigg\}\exp i(k_{xe}^{pf}x + k_{ze}^{pf}z - \omega\tau). \tag{19b}$$

The backward-propagating SHG is described by solutions to the equations

$$(n_o^{sf})^2\partial_{xx}^2 E_x^{f^-} + (n_e^{sf})^2\partial_{zz}^2 E_x^{f^-} + (kn_e^{sf}n_o^{sf})^2 E_x^{f^-}$$
$$= -(E_x^{pf^-})^2\chi_{31}^{(2)}k^2\Bigg\{[(n_e^{sf})^2$$
$$- (n(\theta_e^{pf})\sin\theta_e^{pf})^2]2\left(\frac{n_o^{pf}}{n_e^{pf}}\right)^2\tan\theta_e^{pf}$$
$$- [n(\theta_e^{pf})]^2\left\{1 + \frac{\chi_{33}^{(2)}}{\chi_{31}^{(2)}}\left[\left(\frac{n_o^{pf}}{n_e^{pf}}\right)^2\tan\theta_e^{pf}\right]^2\right\}\cos\theta_e^{pf}\sin\theta_e^{pf}\Bigg\}$$
$$\times \exp i[k_{xe}^{pf}x + k_{ze}^{pf}(L - z) - \omega\tau], \tag{20a}$$

and
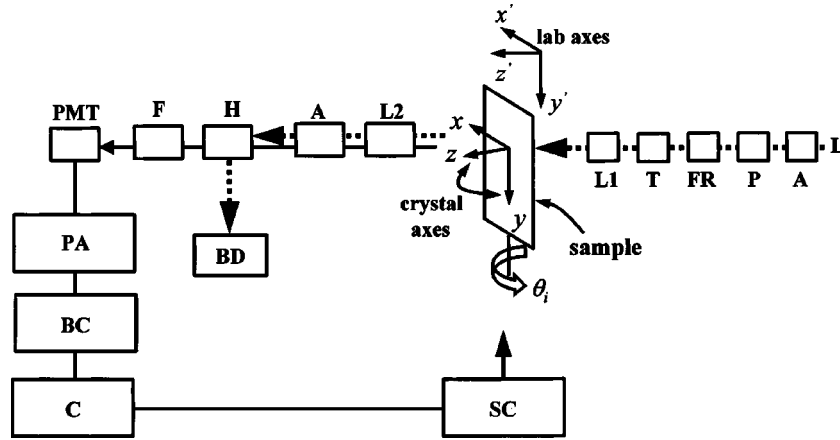
FIG. 2. A schematic showing the apparatus used to generate and record rotational Maker fringes from the $Al_xGa_{1-x}N$ samples. L is the output of the mode-locked Q-switched laser; A is the attenuator used to set the power incident on the sample; P is a polarizer that sets the polarization fidelity of the input pump beam (shown as a dashed line); FR is a glass Fresnel rhomb to set the state of polarization of the pump beam on the sample; T is a telescope to expand and collimate the pump beam; $L1$ is a lens to focus the pump on the sample; $L2$ is a lens that collects and collimates the SHG (shown as a solid line) and residual pump beam (dashed); A is an analyzer to select the state of polarization of the SHG; H is a harmonic beam splitter to reject the residual pump beam; BD is a beam dump for the residual pump beam; F is a 532 nm bandpass filter; PMT is a photomultiplier tube for detecting the SHG; PA is a current-sensitive preamplifier; BC is a boxcar averager; C is a computer that records the SHG data and controls the stage motion; SC is the control electronics for the rotation/translation stage system; θ_i is the pump angle of incidence; x', y', and z' are the lab axes fixed with respect to the pump beam; x, y, and z are the crystal axes.

$$(n_o^{sf})^2 \partial_{xx}^2 E_z^{f^-} + (n_e^{sf})^2 \partial_{zz}^2 E_z^{f^-} + (k n_e^{sf} n_o^{sf})^2 E_z^{f^-}$$

$$= (E_x^{pf^-})^2 \chi_{31}^{(2)} k^2 \left\{ \left\{ 1 + \frac{\chi_{33}^{(2)}}{\chi_{31}^{(2)}} \left[\left(\frac{n_o^{pf}}{n_e^{pf}} \right)^2 \tan \theta_e^{pf} \right] \right\}^2 \right.$$

$$\times [(n(\theta_e^{pf}) \cos \theta_e^{pf})^2 - (n_o^{sf})^2] - 2 \left[\frac{n(\theta_e^{pf}) n_o^{pf} \sin \theta_e^{pf}}{n_e^{pf}} \right]^2 \right\}$$

$$\times \exp i[k_{xe}^{pf} x + k_{ze}^{pf}(L-z) - \omega\tau]. \tag{20b}$$

The general solutions to Eqs. (19a), (19b), (20a), and (20b) are

$$E_x^{f^+} = E_x^{f_o^+} \exp i(k_{xe}^{sf} x + k_{ze}^{sf} z - i\omega\tau)$$
$$+ A_x^+ \exp i(k_{xe}^{pf} x + k_{ze}^{pf} z - \omega\tau), \tag{21a}$$

$$E_z^{f^+} = E_z^{f_o^+} \exp i(k_{xe}^{sf} x + k_{ze}^{sf} z - i\omega\tau)$$
$$+ A_z^+ \exp i(k_{xe}^{pf} x + k_{ze}^{pf} z - \omega\tau), \tag{21b}$$

$$E_x^{f^-} = E_x^{f_o^-} \exp i[k_{xe}^{sf} x + k_{ze}^{sf}(L-z) - i\omega\tau]$$
$$+ A_x^- \exp i[k_{xe}^{pf} x + k_{ze}^{pf}(L-z) - \omega\tau], \tag{21c}$$

$$E_z^{f^-} = E_z^{f_o^-} \exp i[k_{xe}^{sf} x + k_{ze}^{sf}(L-z) - i\omega\tau]$$
$$+ A_z^- \exp i[k_{xe}^{pf} x + k_{ze}^{pf}(L-z) - \omega\tau]. \tag{21d}$$

The coefficients A_x^+, A_z^+, A_x^-, A_z^- for this e-e case are found by substitution of Eqs. (21a) and (21b) into Eqs. (19a) and (19b) and substitution of Eqs. (21c) and (21d) into Eqs. (20a) and (20b). Note that the e-polarized pumping condition is distinguished by the "e" subscript appearing on the wave vector components k_{xe}^{pf} and k_{ze}^{pf}. In an analogous fashion to Sec. II C, we solve for the amplitude of transmitted SHG field E_x^{sa} for this e-e pumping case and arrive at an expression for the

normalized SHG output power $\mathbf{P}_{ee}^A = |\mathbf{E}_e^{sa}|^2$. An explicit form of $|\mathbf{E}_e^{sa}|^2$ is given in Appendix B.

III. EXPERIMENTAL RESULTS

A schematic of the apparatus and data-acquisition system used to collect Maker fringes is illustrated in Fig. 2. Data were collected from the series of thin-film $Al_xGa_{1-x}N$ and bulk GaN samples in the following manner. The samples were separately mounted on an automated rotation/translation positioning system that also held a crystalline quartz reference plate in close proximity to the sample under test. The y-cut quartz reference plate was 0.501 mm thick and 25 mm in diameter. The pump beam was derived from a mode-locked (82 MHz) Q-switched (800 Hz) Nd:YAG laser operating at 1064 nm. The pump beam falling on the sample was approximately 70 μm in diameter and the average power was typically attenuated to 30 mW. The polarization of the pump was set using a glass Fresnel rhomb. The optical system was checked carefully to insure that no spurious SHG artifacts were generated by the pump steering, focusing, and polarization optics. Maker fringes were collected in repetitive succession from a sample and the reference plate under identical conditions of pump intensity. The laser was sufficiently stable so that continuous monitoring of the pump intensity during data collection was unnecessary. This was verified by checking the consistency of the repetitive data sets collected from both the sample under test and the reference plate over a period of several minutes. The c axis of the reference plate was set parallel to the laboratory y axis (sample stage rotation axis labeled as the y' axis in Fig. 2) and the pump and SHG polarization were parallel to the laboratory x axis (labeled as x' in Fig. 2) for all Maker fringe scans of the reference plate. The o-e cases necessitated switching the pump polarization from y' to x' (laboratory frame) as the stage alternated between placing the sample
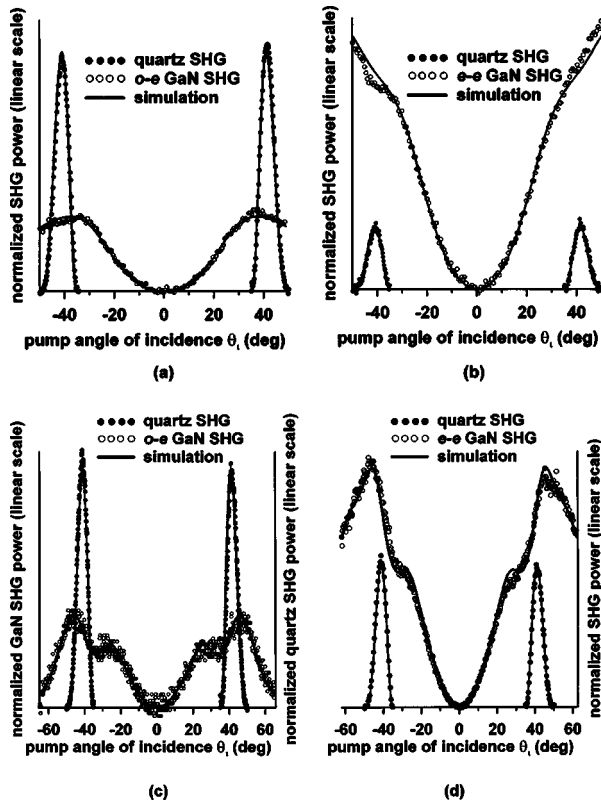
FIG. 3. (a) Data and simulation of Maker fringes for the *o-e* pumping case for the MOCVD grown GaN sample. Superimposed on the graph are the data and simulations for the corresponding quartz reference scan. The GaN and quartz SHG data are on the same scale. (b) Data and simulation of Maker fringes, and corresponding quartz SHG reference scan, for the *e-e* pumping case are shown for the sample illustrated in (a). The GaN and quartz SHG data are on the same scale, but the scale is not the same as that used in (a). (c), (d) Similar to (a), (b) but results for the 4.4 μm thick HVPE grown GaN sample are shown.

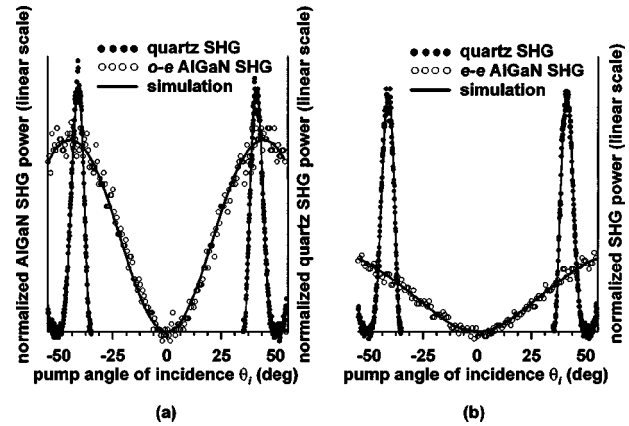
FIG. 4. (a) Data and simulation of Maker fringes for the *o-e* pumping case, and corresponding quartz SHG reference scan for the MOCVD grown Al$_x$Ga$_{1-x}$N sample with $x=0.618$. The quartz and Al$_x$Ga$_{1-x}$N data are displayed on different scales because of the relatively weaker SHG output resulting from this pump orientation for this high value of x. (b) Data and simulation of Maker fringes, and corresponding quartz SHG reference scan, for the *e-e* pumping case for the sample illustrated in (a). The Al$_x$Ga$_{1-x}$N and quartz SHG data are displayed on the same scale in this case.

under test or the quartz reference plate in the focus of the pump beam. The theoretical modeling of the SHG produced by the quartz reference plate was performed in a manner similar to the approach used in Sec. II, and the result is essentially indistinguishable from the earlier results of Jerphagnon and Kurtz.[17]

It was necessary to establish an accurate value of sample thickness L in order to properly fit the Maker fringes and calculate the nonlinear coefficients of the Al$_x$Ga$_{1-x}$N films and bulk GaN samples. Using the previously established values for refractive index and birefringence as input,[10] the sample thickness L at the location of a Maker fringe scan was calculated by least-squares fitting of the simulation to the *o-e* Maker fringe data. The prism-coupling methods that were used to measure refractive index of the Al$_x$Ga$_{1-x}$N films also permit computation of L. However, variation in film thickness of a few tens of nanometers between points on a sample separated by a few millimeters was not uncommon. Since it was impossible to insure that the Maker fringe scans were performed at precisely the same location at which the prism coupling measurements were made, it was necessary to compute L directly from the Maker fringe data. Furthermore, for the the thicker bulk samples prism-coupling meth-

ods are impractical, so use of the Maker fringe data to establish sample thickness is one of the few nondestructive options available.

With L established, $\chi_{31}^{(2)}$ was calculated using a least-squares fitting procedure that scaled the amplitude of the *o-e* Maker fringe data with respect to the adjacent scans from the quartz reference plate. The Maker fringes from the *e-e* case depend upon L, $\chi_{31}^{(2)}$, $\chi_{33}^{(2)}$ and refractive index. Using the previously computed value of L as input, both $\chi_{31}^{(2)}$ and $\chi_{33}^{(2)}$ were varied as independent parameters in a least-squares procedure to fit the simulation to these data. This also provided a separate check of the consistency of the results for $\chi_{31}^{(2)}$. Examples using these procedures for fitting the simulations to the *o-e* and *e-e* data for the thin MOCVD- and HVPE-grown GaN samples (Al$_x$Ga$_{1-x}$N with $x=0$) are shown in Figs. 3(a)–3(d). For the MOCVD sample, a fit for the *o-e* case that also superimposes Maker fringe data and simulation for the quartz reference SHG, is given in Fig. 3(a). A fit for the *e-e* case is illustrated in Fig. 3(b). Figures 3(c) and 3(d) illustrates similar results for the thin HVPE grown GaN sample. Graphs illustrating the results for the MOCVD-grown sample with $x=0.618$ are given in Figs. 4(a) and 4(b). The results for the computed values of L, $\chi_{31}^{(2)}$, $\chi_{33}^{(2)}$, and the values of refractive index that were used in the computations for all of the thin film samples, are given in Table I. In order to illustrate the consistency of the solutions for $\chi_{31}^{(2)}$ as derived from the *o-e* and *e-e* simulations, the table lists values of $\chi_{31}^{(2)}$ computed from both cases. These fitting procedures will not allow absolute determination of the sign of $\chi_{31}^{(2)}$ with respect to $\chi_{11}^{(2)}$ (quartz) since $|\mathbf{E}_e^{sa}|^2$ is proportional to $[\chi_{31}^{(2)}]^2$ (for both the *o-e* and *e-e* cases). We can determine only the relative sign of $\chi_{31}^{(2)}$ with respect to $\chi_{33}^{(2)}$. This point is discussed further in Ref. 11. In order to maintain the convention established by previous authors, e.g. Ref. 4, we assume that the sign of $\chi_{31}^{(2)}$ is positive.

There is a range of reported results for the value of the quartz $\chi_{11}^{(2)}$ coefficient.[18,19] In our previous work with recon-

TABLE I. A summary of the computed values of the nonlinear coefficients $\chi_{31}^{(2)}$ and $\chi_{33}^{(2)}$ is given for the GaN and Al$_x$Ga$_{1-x}$N samples. The reference level was set using $\chi_{11}^{(2)}$ (quartz)=0.64 pm/V. The listed values of the refractive indices n_o^{pf}, n_e^{pf}, n_o^{sf}, and n_e^{sf} were used to fit the simulations to the Maker fringe data in computations of the nonlinear coefficients. As indicated in our earlier paper (Ref. 10), samples with x=0.279 and 0.363 each supported only one extraordinary-polarized guided mode at 1064 nm, consequently a reliable value for n_e^{pf} could not be evaluated at this wavelength. The lack of n_e^{pf} precluded computation of $\chi_{33}^{(2)}$ for these two samples. The values of sample thickness L computed from fitting the o-e data are also given in the table. The "U," "H," and "M," designations in the first column refer, respectively, to crystal growth by high-pressure, HVPE, and MOCVD methods. The first two samples were free-standing while all of the other samples remain on their (0001) sapphire growth substrates. The estimated uncertainty in $\chi_{31}^{(2)}$ is ±8% and the estimated uncertainty in $\chi_{33}^{(2)}$ is ±40%. The consistency of the computation of $\chi_{31}^{(2)}$ via the o-e and e-e simulations is indicated in the second and third columns.

x	$\chi_{31}^{(2)}$ (oe)	$\chi_{31}^{(2)}$ (ee)	$\chi_{33}^{(2)}$	n_o^{pf}	n_e^{pf}	n_o^{sf}	n_e^{sf}	L (μm)
0.000 (U)	5.3	5.3	−8.0	2.3040	2.3420	2.3970	2.4350	160.14
0.000 (H)	5.7	5.5	−9.2	2.3039	2.3372	2.3970	2.4350	229.67
0.000 (H)	5.8	5.8	−20.6	2.3040	2.3373	2.3970	2.4350	69.70
0.000 (H)	5.7	5.8	−10.4	2.3040	2.3373	2.3970	2.4350	4.400
0.000 (M)	5.3	5.5	−7.4	2.3040	2.3420	2.3970	2.4350	2.134
0.279 (H)	4.0	⋯	⋯	2.2190[a]	⋯	2.3080	2.3400	2.426
0.363 (H)	3.0	⋯	⋯	2.2170[a]	⋯	2.2780	2.3160	0.443
0.419 (M)	3.0	3.2	−6.4	2.2100	2.2360	2.2720	2.3080	1.317
0.507 (M)	2.4	2.6	−1.8	2.1820	2.2160	2.2460	2.2820	1.181
2.593 (H)	1.9	2.1	−0.9	2.1570	2.2000	2.2150	2.2510	0.581
0.618 (M)	1.8	2.1	−0.7	2.1550	2.1930	2.2120	2.2480	0.954
0.660 (M)	1.7	1.9	−0.6	2.1470	2.1800	2.2020[b]	2.2340[b]	1.022
0.666 (M)	1.6	1.7	3.9	2.1440	2.1820	2.1990	2.2340	1.018

[a]These values of p_o^{nf} were computed using the two-term Sellmeier equations of Ref. 10.
[b]These values of n_o^{sf} and n_e^{sf} were extrapolated from prism-coupling data presented in Ref. 10.

ciling the nonlinear coefficients of LiNbO$_3$ and quartz,[20] we concluded that the correct value of $\chi_{11}^{(2)}$ for quartz is 0.64 pm/V±8% and we used this result to set the scale of the GaN and Al$_x$Ga$_{1-x}$N nonlinear susceptibilities in the present work. Since the amplitude of the o-e Maker fringes are directly proportional to $[\chi_{31}^{(2)}]^2$, the corresponding uncertainty $\chi_{31}^{(2)}$ is identical to the uncertainty of $\chi_{11}^{(2)}$ (quartz). The uncertainty in refractive index of ±0.005 (as given in Ref. 10) does not contribute substantial additional uncertainty to computations of $\chi_{31}^{(2)}$ for these thin-film samples. The simulations reveal that the e-e Maker fringes depend primarily on $\chi_{31}^{(2)}$ and depend comparatively weakly on $\chi_{33}^{(2)}$. The uncertainty for $\chi_{33}^{(2)}$ was estimated by propagating the uncertainty of $\chi_{11}^{(2)}$ (quartz) through the least-squares fitting procedure for the e-e case and including the additional effects of the uncertainty in refractive index on the calculation. Using this procedure we estimate that the typical uncertainty in $\chi_{33}^{(2)}$ is ±40%. The plotted values of $\chi_{31}^{(2)}$ in Fig. 5 are those derived from fitting the o-e simulation with the corresponding Maker fringe data (column 2 of Table I). Column 3 of Table I lists the values of $\chi_{31}^{(2)}$ that were derived using the fitting procedure for the e-e case. The plotted values of $\chi_{33}^{(2)}$ in Fig. 5 are taken from column 4 of Table I. Also included in Fig. 5 are the experimental values of $\chi_{31}^{(2)}$ and $\chi_{33}^{(2)}$ for AlN given by Refs. 21 and 22, and the theoretical values for these quantities, for both GaN and AlN, given by Ref. 11. Note that in Fig. 5 the data of Ref. 21 have been scaled using $\chi_{11}^{(2)}$ (quartz)=0.64 pm/V.

For the thicker GaN samples, whose thicknesses are relatively large compared to the coherence length for second harmonic generation, the Maker fringe patterns are sensitive to changes in refractive index on the order of ±0.0001. For the o-e case the coherence length l_c^{oe} is defined by $l_c^{oe}=\lambda/2|n_o^{pf}-n(\theta_e^{sf})|$, and the coherence length for the e-e case

l_c^{ee} is given by $l_c^{ee}=\lambda/2|n(\theta_e^{pf})-n(\theta_e^{sf})|$. As an approximate numerical example, in most instances $n(\theta_e^{pf})\sim n_o^{pf}$ and $n(\theta_e^{sf})\sim n_o^{sf}$ so that $l_c^{oe}\sim l_c^{ee}\sim 2.9$ μm. As given in the Appendix, the oscillatory dependence of the o-e Maker fringes is proportional to $\cos k[n_o^{pf}-n(\theta_e^{sf})]L$, or $\cos(L\pi/l_c^{oe})$, with similar expressions for the e-e case. For $L\sim 230$ μm (approximate thickness of the free-standing HVPE grown sample), a variation in the argument of $\cos(L\pi/l_c^{oe})$ by $\pi/10$ (resulting in a readily observable shift of the Maker fringe pattern) will be induced by a variation in $(n_o^{pf}-n_e^{sf})$ of roughly 10^{-4}. On the other hand, for a sample ~ 1 μm thick, a variation in $(n_o^{pf}-n_e^{sf})$ by roughly 0.03 is necessary to induce a shift of $\pi/10$ in the argument of $\cos(L\pi/l_c^{oe})$. As discussed in Ref.
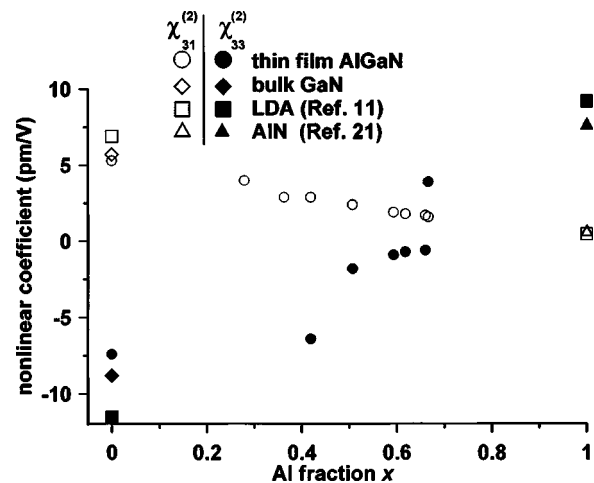

FIG. 5. Graph illustrating $\chi_{31}^{(2)}$ and $\chi_{33}^{(2)}$ as a function of Al fraction x. Also included are results for the bulk free-standing HVPE grown GaN plate, the theoretical results for GaN and AlN given by Ref. 11, and the experimental results for AlN given by Refs. 21 and 22. Note that the data of Ref. 21 are scaled by choosing $\chi_{11}^{(2)}$(quartz)=0.64 pm/V.
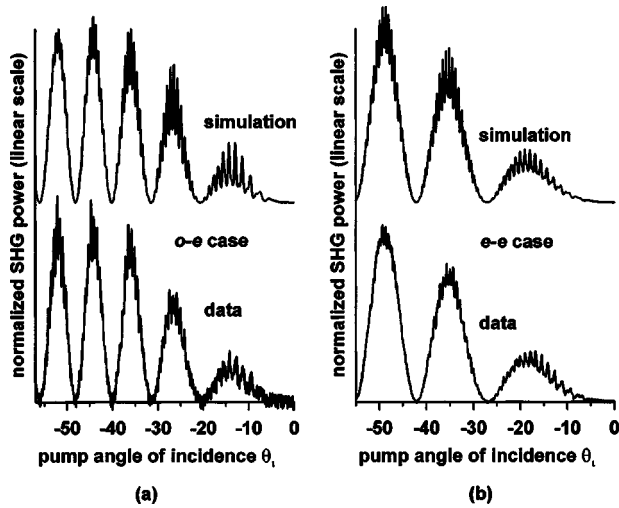
FIG. 6. Maker fringes and simulations for the bulk free standing HVPE grown GaN sample. For clarity, the graphical results are displaced vertically, the quartz reference scans are omitted, and only portions of the θ_i ranges are displayed: (a) data and simulation for the *o-e* pumping case and (b) data and simulation for the *e-e* pumping case.

10, the estimated uncertainty in the refractive index data derived by prism coupling methods that appear in Table I is ±0.005. Therefore, this level of precision in the refractive indices is generally adequate for fitting the simulation to the Maker fringe data for the thin AlGaN samples for computation of $\chi_{31}^{(2)}$ via the *o-e* case. On the other hand, the *e-e* simulation reveals a relatively weak sensitivity to $\chi_{33}^{(2)}$ on the corresponding Maker fringes. Thus for the *e-e* case, variations in refractive index on the order of ±0.005 emerge as variations in computed values of $\chi_{33}^{(2)}$ by roughly ±40% as discussed earlier.

Given the sensitivity of the *o-e* and *e-e* Maker fringe simulations to small changes in refractive index for relatively thick samples, fitting the simulations to the Maker fringe data for the thick GaN samples could sometimes be improved by varying the refractive index values from those appearing in Ref. 10. For example, Fig. 6(a) illustrates the *o-e* case for fitting the simulation to the data for the freestanding HVPE sample and the corresponding *e-e* case is illustrated in Fig. 6(b). The modified values of refractive index used to obtain these fits are given in row 2 of Table I and fall within the ±0.005 uncertainty for the refractive index data derived from prism coupling. For clarity, the simulations are displaced from the data in Figs. 6(a) and 6(b). Note that the visibility of the high-frequency Maker fringe data is represented fairly well by the simulation. Fitting the simulation to the *o-e* data yields a value of thickness L =229.67±0.2 μm. Scaling the *o-e* data to the quartz reference using the least-squares procedure gives $\chi_{31}^{(2)}$ =5.7 pm/V. Scaling of the *e-e* SHG data yields a value of $\chi_{33}^{(2)}$=−9.2 pm/V. The uncertainties in these quantities were estimated to be the same as those computed for the thin-film samples.

As illustrated in Fig. 7(a), results for the ~70 μm thick HVPE GaN sample permits a clearer illustration of the fit of the high-frequency Maker fringes for the *o-e* case, although the simulation suggests that the visibility of the high-
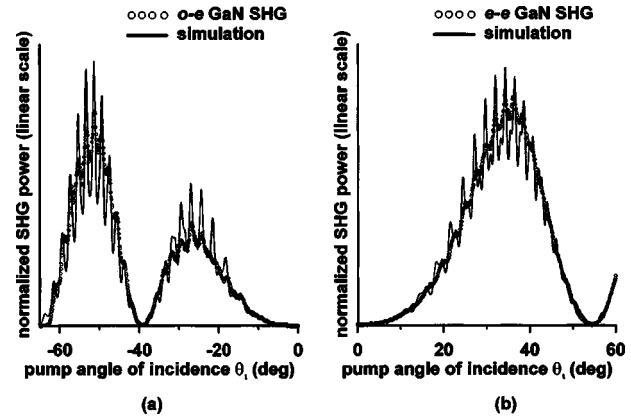

FIG. 7. Maker fringes and simulations for the 69.7 μm thick HVPE GaN sample remaining on its sapphire substrate. For clarity, the reference data is omitted and only portions of the θ_i ranges are displayed: (a) data and simulation for the *o-e* pumping case and (b) data and simulation of the *e-e* pumping case. Although resolvable, the visibility of the high-frequency Maker fringes is much less than predicted by the simulation.

frequency fringe data is less than expected. This fit was obtained using values for n_o^{pf}, n_o^{sf}, and n_e^{sf} from Ref. 10. As illustrated in Fig. 7(b), the reduced visibility of the high frequency fringes for the *e-e* case is even more pronounced, although the simulation locates the positions of the fringes quite well. As noted in Table I, the fit for the *e-e* case was facilitated by varying n_e^{pf} from its value as determined by prism-coupling analysis,[10] while the values for n_o^{pf}, n_o^{sf}, and n_e^{sf} were the same as those for the *o-e* case. Note that the *o-e* fit does not require n_e^{pf}. The computed value for $\chi_{31}^{(2)}$ appears reasonable compared to the results for the other GaN samples, but the computed value for $\chi_{33}^{(2)}$ differs from that of the other GaN samples by roughly a factor of 2. We will comment on this discrepancy in Sec. IV. Finally, the results for the bulk high-pressure grown sample are illustrated in Figs. 8(a) and 8(b) and Table I.

IV. DISCUSSION

A survey of the literature reveals a range of reported numerical values of $\chi_{31}^{(2)}$ and $\chi_{33}^{(2)}$ of GaN[4,23,24] and no data (as
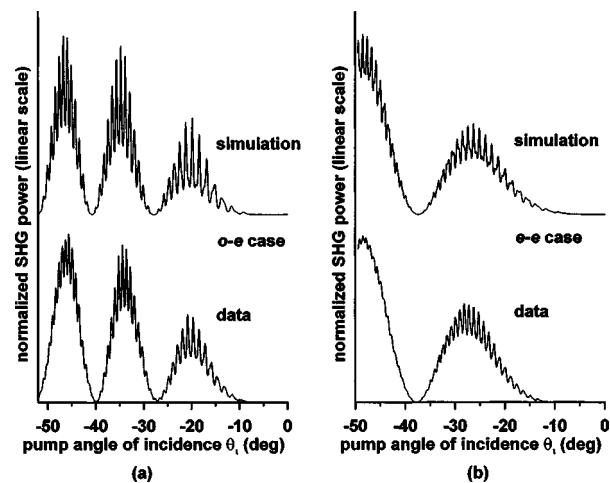

FIG. 8. Maker fringes and simulations for the bulk free-standing high-pressure-grown GaN sample. For clarity, the graphical results are displaced vertically, the quartz reference scans are omitted, and only portions of the θ_i ranges are displayed: (a) data and simulation for the *o-e* pumping case and (b) data and simulation of the *e-e* pumping case.

far as we are aware) on these quantities for $Al_xGa_{1-x}N$. For example, in their NLO studies of GaN, Zhang *et al.*[23] give $d_{31}=8.2\pm0.7$ pm/V and $d_{33}=-16.5\pm1.3$ pm/V (respectively, corresponding to $\chi^{(2)}_{31}=16.4\pm1.4$ and $\chi^{(2)}_{33}=-33.0\pm2.6$ pm/V). For the quartz reference, the authors used $d_{11}=0.3$ pm/V ($\chi^{(2)}_{11}=0.6$ pm/V). Also, Kravetsky *et al.*[24] give $d_{31}=5.46$ pm/V and $d_{33}=-11.07$ pm/V for GaN. In their extensive summary NLO study of GaN, Miragliotta *et al.*[4] give various examples of $\chi^{(2)}_{31}$ that range from 4.22 to 4.8 pm/V, and values of $\chi^{(2)}_{33}$ that range from -8.82 to -9.59 pm/V. Our results for both the thin-film and bulk free-standing GaN samples agree more closely with those of Refs. 4 and 24. However, we find within experimental error that the expected constraint that $\chi^{(2)}_{33}=-2\chi^{(2)}_{31}$ is obeyed only loosely given the inherent uncertainties in the measurements and simulations. Moreover, this constraint is not rigorously verified in computations of these nonlinear susceptibilities derived from the Kohn–Sham local-density approximation (LDA).[11]

Note that the surfaces of both the free-standing HVPE-grown and high-pressure grown samples were prepared by mechanical polishing. This was necessary to remove damage induced during the substrate removal process for the former, and to eliminate irregular features from as-grown faces on the latter.[12] The visibility of the high-frequency Maker fringes displayed by each sample reveals that the surface quality is quite good. The high-pressure-grown sample, however, displayed thickness variations on the order of 0.1 μm over an area roughly 0.3 mm^2. Even with careful alignment, it was quite difficult to place the sample rotation axis precisely on the pump focus spot. Consequently, as θ_i was scanned, the pump beam would typically sweep across roughly 0.3 mm of the sample while the Maker fringe data was collected, and if the sample thickness varies over this range, the variation will be revealed by an asymmetric spacing of the Maker fringes.

Comparison of the results for the free-standing GaN samples to those for the ~70 μm thick HVPE GaN sample (remaining on its growth substrate) shows that the latter displays a pronounced reduction in the visibility of the high-frequency Maker fringes, particularly for the *e-e* case. We attribute this effect due to irregularities at the growth interface. The simulation routines return a value for $\chi^{(2)}_{31}$ that is consistent with the other GaN samples, and locate the positions the remnant high frequency fringes for the *e-e* case. However, in comparison to the other GaN samples, an anomalously large negative value of $\chi^{(2)}_{33}$ is computed. It is doubtful that this result is physically reasonable since the inherently weak dependence of the *e-e* Maker fringes on $\chi^{(2)}_{33}$, coupled with the reduced visibility and perturbations in the envelope of the high frequency *e-e* Maker fringe data, could lead to such a numerical artifact. Taken together, the results for the thick samples illustrate the need for good resolution of both high- and low-frequency Maker fringe data in order to fit the simulations.

The observed trend of the reduction in the $\chi^{(2)}_{31}$ with increasing Al content for the thin film samples is consistent with reports of the comparatively small magnitude of this coefficient for AlN.[21,22] Furthermore, the equality of the signs of $\chi^{(2)}_{31}$ and $\chi^{(2)}_{33}$ has also been reported for AlN.[21,22] For example, in their SHG studies of single-crystal AlN films formed by reactive evaporation on sapphire substrates, Fujii *et al.*[21] give the approximate values: $|d_{33}|=23.2d_{11}$(quartz) and $|d_{31}|\leqslant0.04|d_{33}|$. These results are in reasonable agreement with the work of Kiehne *et al.*[22] on sputter-deposited AlN films. Additionally, LDA computations of the second-harmonic susceptibilities offer theoretical agreement to the observations that the signs of $\chi^{(2)}_{31}$ and $\chi^{(2)}_{33}$ are equal in AlN.[11] Our results also demonstrate that at an Al composition of roughly 66%, the signs of $\chi^{(2)}_{31}$ and $\chi^{(2)}_{33}$ become equal, indicating that this effect occurs well below a purely AlN composition. Arguing from the point of view of bond-charge theory[25,26] Fujii *et al.*[21] have speculated that distortions of the AlN tetrahedra may explain the observed trends in $\chi^{(2)}_{31}$ and $\chi^{(2)}_{33}$. Our own x-ray diffraction studies confirm that the $Al_xGa_{1-x}N$ samples are under in-plane compressive strain.[27] However, the results of the LDA studies indicate that the computed results for the nonlinear susceptibilities for AlN should persist whether or not the AlN tetrahedra were distorted from their ideal structure.[11]

V. CONCLUSIONS

Rotational Maker fringes were used to measure the nonlinear susceptibilities $\chi^{(2)}_{31}$ and $\chi^{(2)}_{33}$ for a series of MOCVD and HVPE $Al_xGa_{1-x}N$ thin-film samples grown on sapphire substrates with x ranging from 0 to 0.666. Over this composition range, $\chi^{(2)}_{31}$ was found to vary from approximately 5.3 pm/V (for $x=0$) to 1.6 pm/V (for $x=0.666$), while $\chi^{(2)}_{33}$ varied from -7.4 to 3.9 pm/V over the same range in x. The estimated uncertainty in $\chi^{(2)}_{31}$ is $\pm8\%$ and the estimated uncertainty in $\chi^{(2)}_{33}$ is $\pm40\%$. The reduction in the magnitude of $\chi^{(2)}_{31}$ and sign reversal of $\chi^{(2)}_{33}$ with increasing x are consistent with experimental results for AlN published by other workers.[21,22] Our data indicate that the equality in the signs of $\chi^{(2)}_{31}$ and $\chi^{(2)}_{33}$ occurs near $x=0.66$. Further, our results are also consistent with the theoretical work of Ref. 11 that applied the Kohn–Sham LDA to compute the second-order susceptibilities of GaN and AlN. Examination of a bulk free-standing HVPE-grown GaN sample yielded $\chi^{(2)}_{31}=5.7$ pm/V and $\chi^{(2)}_{33}=-9.2$ pm/V. The Maker fringe data for the thick bulk free-standing samples show good resolution of high-frequency fringes arising from multiple internal reflections of the pump and SHG. This is an indication of crystal homogeneity and nanometer-scale thickness uniformity over the 70 μm pump beam diameter. On the other hand, a sample of ~70 μm thick HVPE GaN (remaining on its growth substrate) showed reduced visibility of the high-frequency Maker fringes, suggesting that interfacial irregularities may play a role in reducing both fringe fidelity and the ability of the simulation procedures to accurately return reasonable estimates of $\chi^{(2)}_{33}$. From an engineering standpoint, we expect our results will help workers in the field to design multilayer stacks of $Al_xGa_{1-x}N$ films with modulated Al composition. Such structures could be useful for the efficient generation of sum- or difference-frequency generation via the modulation of the nonlinear susceptibilities.

APPENDIX A. *O-E* CASE

The normalized power emerging from the substrate is given by $\mathbf{P}_{oe}^A = |\mathbf{E}_e^{sa}|^2$. Also, $|\mathbf{E}_e^{sa}|^2 = |E_x^{sa}|^2 + |E_z^{sa}|^2$ which may also be written as $|\mathbf{E}_e^{sa}|^2 = (|E_x^{sa}|/\cos\theta_i)^2$. Further, $E_x^{sa} = T_e^s E_x^{st}$ and $|E_x^{sa}|^2$ is given by $|D_s/D|^2$ where

$$
\begin{aligned}
|D_s|^2 = |P_1|^2 [& B_1^2 + B_2^2 + B_3^2 + B_4^2 + 2B_1B_2 \cos 2k_{ze}^{sf}L \\
& + 2[B_1B_3 + B_2B_4] \\
& \times \cos(k_{ze}^{sf} - k_{zo}^{pf})L + 2[B_1B_4 + B_2B_3]\cos(k_{ze}^{sf} + k_{zo}^{pf})L \\
& + 2B_3B_4 \cos 2k_{zo}^{pf}L],
\end{aligned} \tag{A1}
$$

$$
\begin{aligned}
|D|^2 = \{ & [(a_1 - a_2)(a_2 + a_4)]^2 + [(a_1 + a_2)(a_4 - a_2)]^2 \\
& - 2[(a_1 - a_2)(a_2 + a_4)][(a_1 + a_2)(a_4 - a_2)] \\
& \times \cos 2k_{ze}^{sf}L\},
\end{aligned} \tag{A2}
$$

and

$$
|P_1|^2 = |(\chi_{31}^{(2)} E_y^{pf^+})^2|^2.
$$

The factors $B_{1\text{-}4}$ are

$$
B_1 = (a_1 - a_2)\{A_1[1 + (R_o^t)^2] + a_2A_3[1 - (R_o^t)^2]\}, \tag{A3}
$$

$$
B_2 = (a_1 + a_2)\{-A_1[1 + (R_o^t)^2] + a_2A_3[1 - (R_o^t)^2]\}, \tag{A4}
$$

$$
B_3 = 2a_2(A_1 - a_1A_3), \tag{A5}
$$

and

$$
B_4 = 2a_2(A_1 + a_1A_3)(R_o^t)^2. \tag{A6}
$$

where $A_1 = n_o^{pf}(\bar{A}_z^+ \sin\theta_o^{pf} - \bar{A}_x^+ \cos\theta_o^{pf})$, $A_3 = \bar{A}_x^+$, $\bar{A}_x^+ = A_x^+/[\chi_{31}^{(2)} \times (E_y^{pf^+})^2]$, and $\bar{A}_z^+ = A_z^+/[\chi_{31}^{(2)}(E_y^{pf^+})^2]$. The factors a_1, a_2, and a_4 are

$$
a_1 = 1/\cos\theta_i, \tag{A7}
$$

$$
a_2 = -\frac{n(\theta_e^{sf})}{\cos\theta_e^{sf}}\left[\left(\frac{n_o^{sf}}{n_e^{sf}}\sin\theta_e^{sf}\right)^2 + (\cos\theta_e^{sf})^2\right], \tag{A8}
$$

and

$$
a_4 = -\frac{n(\theta_e^{st})}{\cos\theta_e^{st}}\left[\left(\frac{n_o^{st}}{n_e^{st}}\sin\theta_e^{st}\right)^2 + (\cos\theta_e^{st})^2\right]. \tag{A9}
$$

To summarize for the *o-e* case

$$
\mathbf{P}_{oe}^A = \left(\frac{\chi_{31}^{(2)}T_e^s}{\cos\theta_i}\right)^2 \left|\frac{D_s}{D}\right|^2. \tag{A10}
$$

Since we only consider Maker fringes of GaN and AlGaN relative to Quartz Maker fringes at the same incident pump power level, we set $E_y^{pi} = 1$ without loss of generality.

For the case of the thick free-standing GaN film, the thickness of the sample ($L = 229.67$ μm) was large compared to the pump beam diameter of 70 μm. Consequently, the multiple internal reflections of the pump and SHG will overlap and interfere to a diminishing amount as θ_i is increased. At the limit of this effect $E_y^{pf^+} \to T_o^i E_y^{pi}$ and the only significant oscillatory term remaining in Eq. (A10) is proportional to $\cos(k_{ze}^{sf} - k_{zo}^{pf})L$. We model this effect in an approximate phenomenological fashion by introducing the damping factor $d_p = \exp[-(4.6\tan\theta_o^{pf})^2]$, which describes the θ_i dependence of the overlap of multiple reflections of the pump, and the damping factor $d_s = \exp[-2(4.6\tan\theta_e^{sf})^2]$, which describes the θ_i dependence of the overlap of multiple reflections of the SHG. The damping factor d_p is applied by replacing $R_o^i R_o^t$ in Eq. (7a) by $d_p R_o^i R_o^t$, and replacing B_2 and B_4 in Eq. (A1) by $d_p B_2$ and $d_p B_4$. The damping factor d_s is applied to Eq. (A2) by replacing $\cos 2k_{ze}^{sf}L$ by $d_s \cos 2k_{ze}^{sf}L$. Use of these damping factors gives a fairly good representation of the envelope of the high-frequency Maker fringes illustrate in Fig. 6(a).

APPENDIX B. *E-E* CASE

Computationally, this case is very similar to the *o-e* case except that the pump is now *e*-polarized. We may use the same form as given in Eqs. (A1)–(A9) with the replacements: $A_1 = (\bar{A}_z^+ \sin\theta_e^{pf} - \bar{A}_x^+ \cos\theta_e^{pf})n(\theta_e^{pf})$, $A_3 = \bar{A}_x^+$, $\bar{A}_x^+ = A_x^+/[\chi_{31}^{(2)}(E_x^{pf^+})^2]$, and $\bar{A}_z^+ = A_z^+/[\chi_{31}^{(2)}(E_x^{pf^+})^2]$. Here it is understood that the factors A_x^+ and A_z^+ are those that apply to the *e-e* case. In the terms B_1, B_2, and B_4, R_o^t is replaced by R_e^t. The factors a_1, a_2, and a_4 are the same for the *o-e* and *e-e* cases. Also, $|\mathbf{E}_e^{pi}|^2 = |E_x^{pi}|^2 + |E_z^{pi}|^2$ so that $|E_x^{pi}|^4 = [|\mathbf{E}_e^{pi}|\cos\theta_i]^4$. To summarize the *e-e* case

$$
\mathbf{P}_{ee}^A = (\chi_{31}^{(2)}T_e^s \cos\theta_i)^2 \left|\frac{D_s}{D}\right|^2. \tag{B1}
$$

Again, since the GaN and AlGaN Maker fringes are scaled relative to quartz Maker fringes using the same incident power, we set $|\mathbf{E}_e^{pi}| = 1$ in our simulations. For application to the thick GaN plate, the damping factor d_s as given above applies for the *e-e* case, but in the argument of the damping factor d_p, θ_o^{pf} is replaced by θ_e^{pf}. Figure 6(b) illustrates fitting the damped *e-e* simulation to the Maker fringe data for the thick free-standing GaN sample.

[1] G. Lüpke, Surf. Sci. Rep. **35**, 75 (1999).
[2] C. Meyer, G. Lüpke, E. Stein von Kamienski, A. Götz, and H. Kurz, Appl. Phys. Lett. **69**, 2243 (1996).
[3] C. K. Sun, S. W. Chu, S. P. Tai, S. Keller, A. Abare, U. K. Mishra, and S. P. DenBaars, Scanning **23**, 182 (2001).
[4] J. Miragliotta, D. K. Wickenden, T. J. Kistenmacher, and W. A. Bryden, J. Opt. Soc. Am. B **10**, 1447 (1993); see also *Semiconductors and Semimetals*, Vol. 57, edited by J. I. Pankove and T. D. Moustakas (Academic, New York, 1999).
[5] D. N. Hahn, G. T. Kiehne, J. B. Ketterson, G. K. L. Wong, P. Kung, A. Saxler, and M. Razeghi, J. Appl. Phys. **85**, 2497 (1999).
[6] L. E. Myers and W. R. Bosenberg, IEEE J. Quantum Electron. **33**, 1663 (1997).
[7] J. Zimmermann, J. Struckmeier, M. R. Hofmann, and J. P. Meyn, Opt. Lett. **27**, 604 (2002).
[8] A. Fragemann, V. Pasiskevicius, G. Karlsson, and F. Laurell, Opt. Express **11**, 1297 (2003).

[9]G. Namkoong, W. A. Doolittle, A. Carver, W. Henderson, D. Jundt, and A. Brown, Proceedings of the 2003 TMS Electronics Materials Conference, Salt Lake City, Utah, June 25–27, 2003, paper CC4.

[10]N. A. Sanford, L. H. Robins, A. V. Davydov, A. Shapiro, D. V. Tsvetkov, A. V. Dmitriev, S. Keller, U. K. Mishra, and S. P. DenBaars, J. Appl. Phys. **94**, 2980 (2003).

[11]J. Chen, Z. H. Levine, and J. W. Wilkins, Appl. Phys. Lett. **66**, 1129 (1995).

[12]The growth and preparation of the thick HVPE sample that was separated from its substrate is described by S. S. Park, I.-W. Park, and S. H. Choh, Jpn. J. Appl. Phys., Part 2 **39**, L1141 (2000); see also E. Oh, S. K. Lee, S. S. Park, K. Y. Lee, I. J. Song, and J. Y. Han, Appl. Phys. Lett. **78**, 273 (2001); Growth of thick HVPE GaN on sapphire is described by R. J. Molnar, Semicond. Semimetals **57**, 1 (1999); Preparation of the bulk high-pressure grown GaN sample is given by S. Porowski and I. Grzegory, *ibid.* **55**, 353 (1998).

[13]P. N. Butcher and D. Cotter, *The Elements of Nonlinear Optics* (Cambridge University Press, New York, 1990).

[14]Y. R. Shen, *The Principles of Nonlinear Optics* (Wiley, New York, 1984).

[15]D. A. Kleinman, Phys. Rev. **126**, 1977 (1962).

[16]F. N. H. Robinson, Phys. Lett. **26A**, 435 (1968).

[17]J. Jerphagnon and S. K. Kurtz, J. Appl. Phys. **41**, 1667 (1970).

[18]V. G. Dmitriev, G. G. Gurzadyan, and D. N. Nikogosyan, *Handbook of Nonlinear Optical Crystals* (Spinger, Berlin, 1991).

[19]I. Shoji, T. Kondo, A. Kitamoto, M. Shirane, and R. Ito, J. Opt. Soc. Am. B **14**, 2268 (1997).

[20]V. Gopalan, N. A. Sanford, J. A. Aust, K. Kitamura, and Y. Furukawa, *Handbook of Advanced Electronic and Photonic Materials and Devices*, edited by H. S. Nalwa, Vol. 4, Ferroelectrics and Dielectrics (Academic, New York, 2001), p. 57.

[21]Y. Fujii, S. Yoshida, S. Misawa, S. Maekawa, and T. Sakudo, Appl. Phys. Lett. **31**, 815 (1977).

[22]P. M. Lundquist, W. P. Lin, Z. Y. Xu, G. K. Wong, E. D. Rippert, J. A. Helfrich, and J. B. Ketterson, Appl. Phys. Lett. **65**, 1085 (1994); see also G. T. Kiehne, G. K. L. Wong, and J. B. Ketterson, J. Appl. Phys. **84**, 5922 (1998).

[23]H. Y. Zhang, X. H. He, Y. H. Shih, M. Schurman, Z. C. Feng, and R. A. Stall, Appl. Phys. Lett. **69**, 2953 (1996).

[24]I. V. Kravetsky, I. M. Tiginyanu, R. Hildebrandt, G. Marowsky, D. Pavlidis, A. Eisenbach, and H. L. Hartnagel, Appl. Phys. Lett. **76**, 810 (2000).

[25]B. F. Levine, Phys. Rev. Lett. **22**, 787 (1969).

[26]B. F. Levine, Phys. Rev. Lett. **25**, 440 (1970).

[27]A. Davydov (unpublished).